

Probing the emission geometry of the X-ray pulsar 2S 1417–624 during a weak outburst with NICER, IXPE, and NuSTAR

M. Zhou¹, P.-J. Wang¹, H.-H. Liu¹, L. Ducci¹, S. S. Tsygankov^{2,1}, Q.-C. Zhao^{3,4}, J. Poutanen², L. Ji⁵, V. F. Suleimanov¹, A. A. Mushtukov⁶, Q. Liu¹, C. M. Diez⁷, L. Abalo⁸, V. Grinberg⁹, and A. Santangelo¹

¹ Institut für Astronomie und Astrophysik, Universität Tübingen, Sand 1, D-72076 Tübingen, Germany
e-mail: pengju.wang@mnf.uni-tuebingen.de, honghui.liu@uni-tuebingen.de

² Department of Physics and Astronomy, 20014 University of Turku, Finland

³ Key Laboratory of Particle Astrophysics, Institute of High Energy Physics, Chinese Academy of Sciences, Beijing 100049, China

⁴ University of Chinese Academy of Sciences, Chinese Academy of Sciences, Beijing 100049, China

⁵ School of Physics and Astronomy, Sun Yat-Sen University, Zhuhai 519082, China

⁶ Astrophysics, Department of Physics, University of Oxford, Denys Wilkinson Building, Keble Road, Oxford OX1 3RH, UK

⁷ European Space Agency (ESA), European Space Astronomy Centre (ESAC), Camino Bajo del Castillo s/n, 28692 Villanueva de la Cañada, Madrid, Spain

⁸ Huygens-Kamerlingh Onnes Laboratory, Leiden University, Postbus 9504, 2300 RA Leiden, The Netherlands

⁹ European Space Agency (ESA), European Space Research and Technology Centre (ESTEC), Keplerlaan 1, 2201 AZ Noordwijk, The Netherlands

–/–

ABSTRACT

We report results from a multi-mission observational campaign of the transient X-ray pulsar 2S 1417–624 during its 2025 outburst, using data from NICER, IXPE, and NuSTAR. Phase-averaged and phase-resolved spectroscopy with NICER and NuSTAR reveal that a typical power-law model with a high-energy cut-off well describes the broadband spectra. Several spectral parameters, however, show clear and systematic modulations with pulse phase, indicating variations in the physical conditions of the emitting plasma over the neutron star’s rotation. In particular, IXPE provides the first polarimetric measurements of this source, yielding a phase-averaged polarization degree of $3.3 \pm 1.7\%$ and a polarization angle of $18^\circ \pm 15^\circ$, both at the 1σ confidence level. Fitting with the rotating vector model yields a magnetic obliquity of $\theta = 64^{+17}_{-26}$ deg, indicating a significantly inclined magnetic geometry that may approach a quasi-orthogonal configuration. Together, these findings demonstrate pronounced phase-dependent spectral and polarization variability, offering valuable constraints on the geometry and emission processes within the accretion region of this transient X-ray pulsar.

Key words. accretion, accretion disks – magnetic fields – polarization – pulsars: individual: 2S 1417–624 – stars: neutron – X-rays: binaries

1. Introduction

Accreting X-ray pulsars (XRPs) are binary systems consisting of a strongly magnetized neutron star ($B \sim 10^{12}$ G) and a companion star. The neutron star accretes material from its companion, releasing gravitational energy and forming highly concentrated emission regions near its magnetic poles (for a review, see Mushtukov & Tsygankov 2024). Constrained by the magnetic field, the infalling matter is channeled along field lines toward the poles, where it forms a hot plasma in the polar cap. The neutron star’s rotation modulates this emission, producing periodic X-ray pulses. The beam pattern depends on the geometry of the emitting regions and the luminosity: in the sub-critical regime, radiation is predominantly emitted along the magnetic axis (“pencil beam”), whereas in the super-critical regime, radiation escapes laterally below the radiation-dominated shock, forming a “fan beam” (Basko & Sunyaev 1975; Becker et al. 2012; Mushtukov et al. 2015). Transitions between these patterns manifest in changes in the pulse profile, pulsed fraction, and spectral properties, highlighting the importance of broadband, long-term monitoring for constraining accretion geometry and emission physics (Reig & Nespoli 2013; Kong et al. 2021; Wang et al. 2022).

Recent advances in X-ray polarimetry have opened a new avenue for probing accreting XRPs. Measurements of the energy and phase dependence of the polarization degree (PD) and polarization angle (PA) can tightly constrain the emission geometry. While PD values in the X-ray band are generally modest (a few to $\sim 10\%$), PA often exhibits a systematic variation with pulse phase. Modeling such variations with the rotating vector model (RVM) can yield the relative orientations of the magnetic axis, spin axis, and the observer’s line of sight (Poutanen 2020; Poutanen et al. 2024). Combined with spectral and pulse profile analyses, polarization measurements can provide direct observations of radiation from the accretion column and probe the neutron star’s magnetic field structure.

2S 1417–624 is a prototypical transient Be/X-ray binary, discovered by SAS-3 in 1978 (Apparao et al. 1980). It has an orbital period of ~ 42.12 d, and an eccentricity e of ~ 0.446 and exhibits coherent X-ray pulsations with a period of ~ 17.64 s (Kelley et al. 1981; Finger et al. 1996). The optical companion is a B1 Ve star (Grindlay et al. 1984). *Gaia* measurements place the system at a distance of $9.9^{+3.1}_{-2.4}$ kpc using the Data Release 2 (Bailer-Jones et al. 2018) and $7.4^{+3.1}_{-1.8}$ kpc using the Data Release 3 (Bailer-Jones et al. 2021), whereas torque modeling suggests a signif-

Table 1. Orbital parameters for 2S 1417–624 (ephemeris adopted from Fermi Gamma-ray Burst Monitor)

Parameter	Value	Unit
Orbital period	42.175	d
$T_{\text{periastron}}$	51612.17000	MJD
$a_X \sin i$	188	light-sec
Longitude of periastron	300.30	deg
Eccentricity	0.4460	

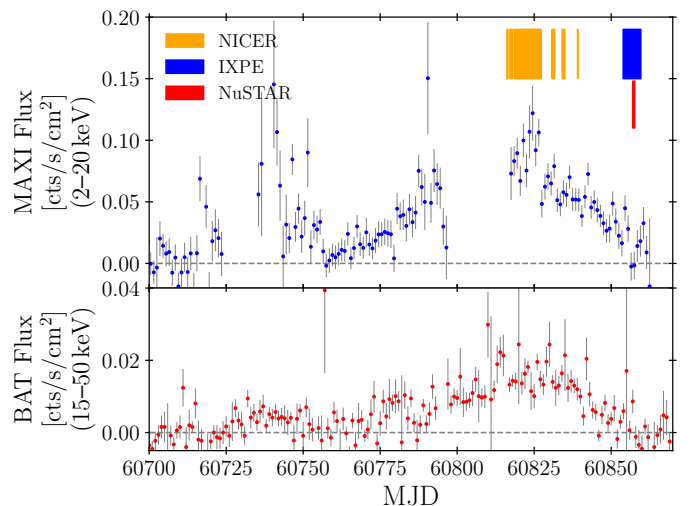
icantly larger distance of ~ 20 kpc (Ji et al. 2020). The surface magnetic field strength of the neutron star is estimated to be $\sim 9 \times 10^{12}$ G, inferred from the cyclotron resonant scattering feature (CRSF) detected at ~ 100 keV (Liu et al. 2024). The source has undergone several bright type-II outbursts in 1994, 1999, 2009, 2018, and 2021, during which the pulse profile, pulsed fraction, and their luminosity dependence show pronounced evolution. For example, the profile can evolve from double- to triple- or quadruple-peaked, and in some cases, the pulsed fraction anticorrelates with luminosity (İnam et al. 2004; Gupta et al. 2018, 2019; Ji et al. 2020; Liu et al. 2024, 2025). In addition to these bright events, the source exhibits lower-luminosity type-I outbursts near periastron, which are shorter in duration and significantly fainter (Finger et al. 1996). Systematic studies of type-I outbursts are scarce, with only a few works (e.g., İnam et al. 2004) analyzing their pulse and spectral properties using 1999–2000 RXTE data.

In this work, we present an analysis of the timing and spectral characteristics of 2S 1417–624 during a new outburst observed in 2025, and report the first X-ray polarization measurement for this source. The remainder of this paper is organized as follows. Section 2 describes the long-term behavior of the source and provides an overview of the data sets analyzed. The main results are presented in Sect. 3, followed by a discussion in Sect. 4. Finally, Sect. 5 summarizes our findings and offers an outlook for future work.

2. Observations and data reduction

2S 1417–624 underwent a new type-II outburst in April 2025, as revealed by continuous monitoring with all-sky X-ray instruments. Figure 1 shows the long-term light curves from MAXI¹ (Matsuoka et al. 2009) in the 2–20 keV band and Swift/BAT² (Barthelmy et al. 2005) in the 15–50 keV band. The maximum brightness reached ~ 70 mCrab in the BAT band around MJD 60825, indicating a significant enhancement in the hard X-ray flux compared to the quiescent level. After the peak, the source began a slow decay, before eventually returning to its pre-outburst flux level. The entire event lasted for roughly two months.

The outburst was observed with the Neutron Star Interior Composition Explorer (NICER; Gendreau et al. 2016), the Imaging X-ray Polarimetry Explorer (IXPE; Weisskopf et al. 2022), and the Nuclear Spectroscopic Telescope Array (NuSTAR; Harrison et al. 2013). An overview of the observations from each X-ray mission, along with the corresponding data reduction procedures, is provided below.

**Fig. 1.** Light curves of 2S 1417–624 during its 2025 outburst as observed by MAXI and Swift/BAT. The observation periods of NICER, IXPE, and NuSTAR are indicated by orange, blue, and red bars, respectively.

2.1. NICER

2S 1417–624 was observed with NICER between May 21 and June 13, 2025 (MJD 60816–60839), near the peak of the outburst, with a total effective exposure time of 27.5 ks. Data reduction was performed with HEASOFT v6.35.2 and the xti20240206 calibration database. The cleaned event lists were generated by the standard nicer12 task, which includes calibration and filtering steps. To minimize the background effects, we applied a custom set of selection criteria to identify good time intervals (GTIs) based on standard NICER screening criteria: an overshoot rate lower than 10 cts per FPM (FPM_OVERONLY_COUNT<10), an undershoot rate lower than 200 cts per FPM (FPM_UNDERONLY_COUNT<200), and a geomagnetic cutoff-rigidity greater than 1.5 GV (COR_SAX>1.5). Spectra were extracted from the resulting GTIs using the tool nicer13-spect. The background spectrum was estimated with model SCORPEON. The energy band for the spectral analyses is 0.7–10 keV.

2.2. IXPE

IXPE is a collaborative project between NASA and the Italian Space Agency, launched aboard a Falcon 9 rocket on December 9, 2021, intending to conduct imaging polarimetry in the 2–8 keV energy range (Weisskopf et al. 2022). The observatory is composed of three identical grazing-incidence X-ray telescopes, each consisting of a mirror module and a polarization-sensitive detector unit (DU) that employs a gas pixel detector (Soffitta et al. 2021; Baldini et al. 2021). For every detected photon, IXPE records its sky position, arrival time, and energy, as well as the emission direction of the associated photoelectron, which is essential for deriving polarization information.

IXPE observed 2S 1417–624 from June 27 to July 3, 2025 (MJD 60853–60859), during which the source was in the final phase of its outburst, with a total effective exposure of 320 ks. During this observation, the data produced by DU2 were unavailable due to pixel failures that had occurred in April 2025 (around MJD 60779). Consequently, our analysis is based solely on the photons detected by DU1 and DU3.

¹ <http://maxi.riken.jp/>

² <https://swift.gsfc.nasa.gov/results/transients/>

The data were processed using the `IXPEOBSSIM` package (version 31.0.3; Baldini et al. 2022) together with calibration files from the calibration database released on July 1, 2024. Before analysis, position offset corrections and energy calibration were applied. Source photons were extracted from a circular region of radius $R_{\text{src}} = 70''$ centered on the target, while the background was estimated from an annular region around the source, defined by inner and outer radii of $R_{\text{in}} = 120''$ and $R_{\text{out}} = 240''$, respectively. In the 2–8 keV energy range, the total source count rate from both available DUs is approximately 0.22 cps, whereas the average background rate in the same band is about 0.001 cps arcmin⁻² per DU. Thus, source photons account for roughly 97% of the total counts within the source region. Given this low background level, no background subtraction was applied when using the `pcube` algorithm provided by the `IXPEOBSSIM` team (Di Marco et al. 2023). Nevertheless, background contributions were included in the spectro-polarimetric analysis performed with `xspec`. The analysis followed the unweighted approach described by Di Marco et al. (2022).

The Stokes I , Q , and U spectra for both available DUs were generated using the unweighted `PHA1`, `PHA1Q`, and `PHA1U` algorithms implemented in the `xpbin` tool of the `IXPEOBSSIM` package. These spectra were then re-binned to ensure a minimum of 30 counts per energy channel, with identical energy binning applied to I , Q , and U . The resulting spectra were fitted simultaneously with the `xspec` package (version 12.15.0; Arnaud 1996) using the IXPE response matrices (`ixpe:obssim20240701:v13`). Fits were performed using χ^2 statistics, and uncertainties are quoted at the 68.3% confidence level (1σ), unless stated otherwise.

We also applied the `pcube` method from the `IXPEOBSSIM` package to carry out a model-independent polarimetric analysis. This approach bypasses the use of the full energy response matrix but incorporates energy dependence by assigning weights to individual photon contributions. All photons within the chosen time interval and energy range were included, and the Stokes parameters were derived via weighted summation (see Eq. 11 in Baldini et al. 2022).

2.3. NuSTAR

NuSTAR observed 2S 1417–624 on July 1, 2025 (MJD 60857) with observation ID 91101319002 and an exposure time of approximately 32.5 ks. We processed the data using `nupipeline` to produce the cleaned event files, and employed `nuproducts` to extract the source and background spectra and light curves. The source region was defined as a circular aperture with a radius of $120''$ centered on the source position, while the background region was chosen as a circular aperture of the same radius located as far from the source as possible.

3. Results

3.1. Pulsar timing studies and the pulse profiles

Before determining the precise pulse period, we first removed the effects of both the Earth’s motion and the binary’s orbital motion. Event arrival times were corrected to the Solar System barycenter using the `barycorr` tool from the `FTOOLS` package. To compensate for orbital motion, we applied additional corrections using the orbital ephemerides provided by the Fermi Gamma-ray Burst Monitor³, which are based on the solutions of Finger et al.

³ <https://gamma-ray.msfc.nasa.gov/gbm/science/pulsars.html>

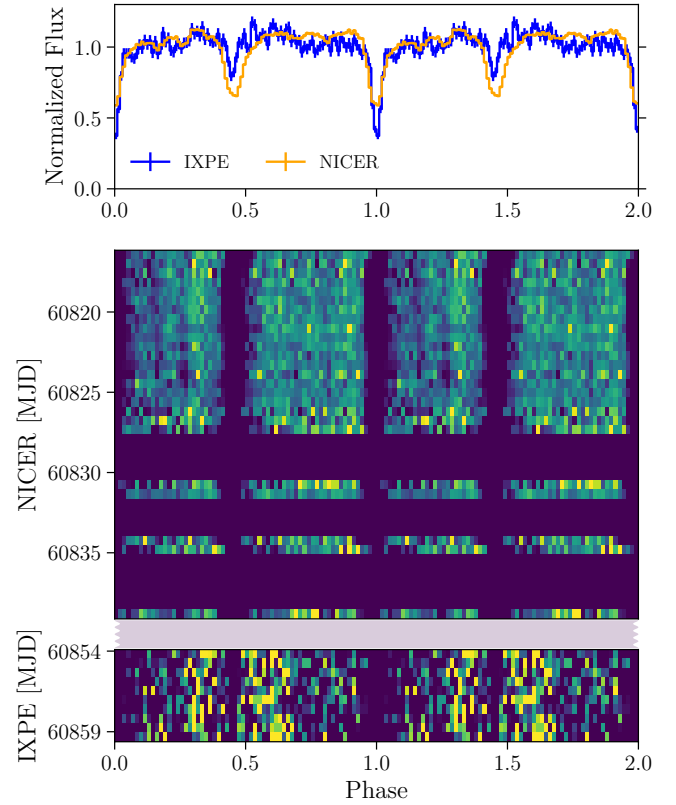


Fig. 2. Pulse profiles of 2S 1417–624 observed by NICER and IXPE, and their phaseograms as a function of time (MJD). Fluxes are normalized to a unit mean. Profiles use 100 phase bins, and phaseograms use 64 phase bins; the phaseograms are divided into 40 time bins for NICER and 10 for IXPE.

(1996) and İnam et al. (2004), but include an adjustment of the orbital period by $-1.25/84$ days, extrapolated to the epoch of the IXPE observation (see Table 1).

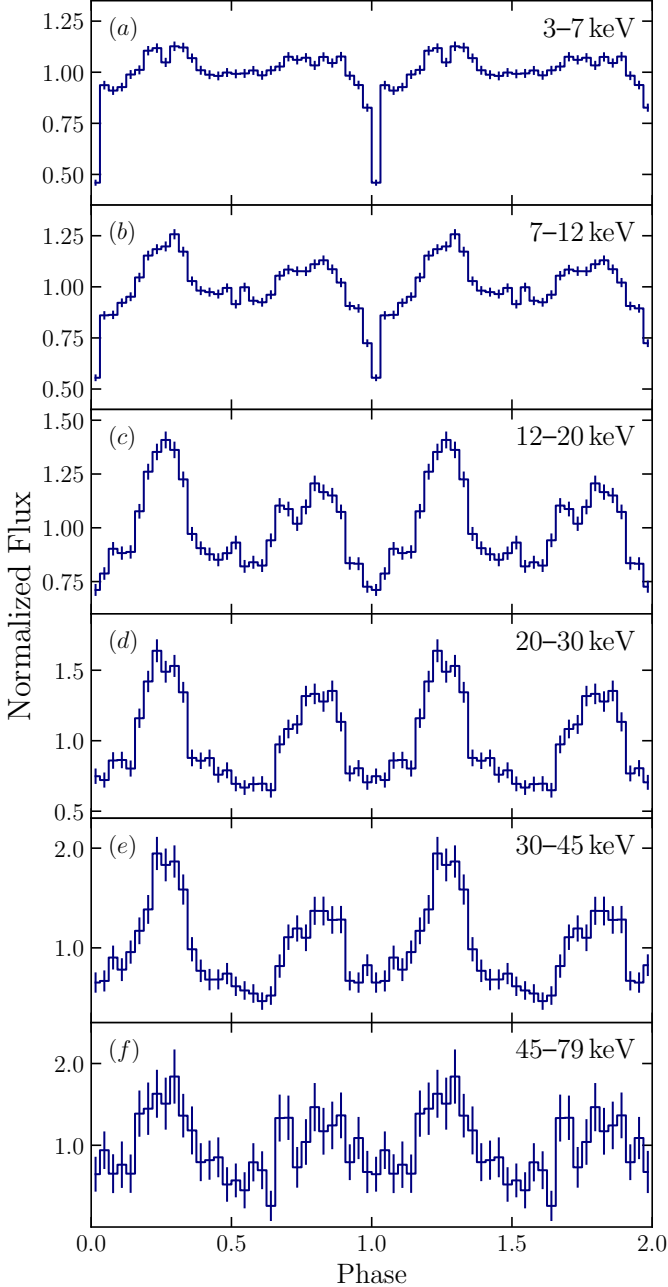
The pulse period (P) and its first derivative (\dot{P}) for the NICER and IXPE data were independently determined using Z^2 statistics with two harmonics (Bucccheri et al. 1983), by maximizing the Z^2 values from all photon events in the 0.7–10 keV band for NICER and the 2–8 keV band for IXPE. The resulting spin parameters and pulse epochs are listed in Table 2. The zero phase of the pulse profile is defined at the phase corresponding to the minimum count rate. Figure 2 shows the NICER and IXPE pulse profiles in their respective energy bands, together with phaseograms tracing pulse profile evolution over 23 days for NICER and 6 days for IXPE. This method naturally maintains phase alignment over extended time spans, as illustrated in Fig. 2. For the NuSTAR data, as the observation lasted less than one day, only the pulse period was determined by maximizing the Z^2 values in the 3–79 keV band, as listed in the last column of Table 2.

The pulse profiles from NICER and IXPE are similar, each showing a prominent dip at phase zero and a shallower dip near phase ~0.45. Both also display two broad peaks, each containing subtle sub-peaks. No significant changes in pulse shape are observed during either observational period. At higher energies, the pulse profile exhibits a sharper double-peaked structure than at lower energies, as indicated by the pulse profile analysis over the broad NuSTAR energy range shown in Figure 3.

Table 2. Pulsar ephemerides of 2S 1417–624 with NICER, IXPE and NuSTAR. The uncertainties are reported at a 1σ confidence level.

Parameter	NICER	IXPE	NuSTAR
Start [MJD]	60816.2	60853.9	60857.0
End [MJD]	60839.1	60859.6	60857.6
Exposure [ks]	27.5	320.2	32.5
t_0 [MJD]	60831.000178 ^a	60857.000098 ^a	60807.945 ^a
Pulse period [s]	17.31294(1)	17.307217(7)	17.3072(1)
Pulse period derivative [10^{-9}s s^{-1}]	-4.36(1)	-1.4(1)	/

Notes. ^(a) The reported reference time t_0 defines the zero phases of the pulse profiles (see Fig. 2).

**Fig. 3.** Pulse profiles at different energies observed by NuSTAR. The fluxes are normalized such that their mean values are unity.

3.2. Spectral analysis

3.2.1. Phase-averaged spectral analysis

NICER’s large effective area in the soft X-ray band ($\sim 1900\text{ cm}^2$ at $\sim 1.5\text{ keV}$) makes it particularly effective for probing soft X-ray emission, whereas NuSTAR’s broader energy coverage, extending up to $\sim 79\text{ keV}$, provides strong constraints on the continuum slope at high energies.

We adopted a systematic error of $\sim 1.5\%$ for all NICER/XTI spectra, as set by default in the `nicer13-spect` tool. All NICER spectra were grouped using the optimal binning method described by [Kaastra & Bleeker \(2016\)](#), ensuring a minimum of 30 counts per bin.

The spectra of 2S 1417–624 in the soft energy band (0.7–10 keV) can be well described by an absorbed power-law with a high-energy cut-off, plus a Gaussian emission line at $\sim 6.4\text{ keV}$ corresponding to the iron fluorescent line. In `XSPEC`, the model can be written as

$$\text{TBabs} \times (\text{cutoffpl} + \text{gaussian}),$$

where TBabs accounts for photoelectric absorption by the interstellar medium, with cross-sections from [Verner et al. \(1996\)](#) and elemental abundances from [Wilms et al. \(2000\)](#). The centroid energy of the gaussian component is fixed at 6.4 keV , while the width parameter σ is constrained to an upper limit of 0.2 keV , corresponding to a narrow iron line.

We first carried out spectral analysis of the phase-averaged data, which provides a more reliable representation of the spectral shape over an extended timescale. A representative spectrum is shown in the upper panel of Fig. 4, and the results of the spectral analysis are presented in Fig. 5. No significant variations are found in the key spectral parameters during the NICER observations, except for the source luminosity, which initially increases and subsequently stabilizes.

For the NuSTAR spectrum, the data were grouped following the same procedure as for NICER. The spectral fitting was performed in the 3–79 keV band. As a first step, we applied the same model used for the NICER data, with a multiplicative constant accounting for the slight normalization differences between FPMA and FPMB. However, this model does not provide an adequate fit to the broad-band spectrum, yielding $\chi^2/\text{d.o.f.} = 589.2/352$. We therefore adopted the model

$$\text{constant} \times \text{TBabs} \times (\text{powerlaw} \times \text{highecut} + \text{gaussian}).$$

which yields a significantly improved fit with $\chi^2/\text{d.o.f.} = 418.1/351$, as shown in the lower panel of Fig. 4. This model is commonly used in spectral analyses of accreting XRPs (see e.g., [Hemphill et al. 2019](#); [Serim et al. 2022](#); [Mandal & Pal 2022](#)). The best-fit parameters are summarized in Table 3.

Table 3. Best-fit spectral parameters from the phase-averaged NuSTAR analysis with the model $\text{constant} \times \text{TBabs} \times (\text{powerlaw} \times \text{highcut} + \text{gaussian})$.

Component	Parameter	Value
TBabs	N_{H} [10^{22} cm^{-2}]	4.25 ± 0.36
powerlaw	Γ	1.10 ± 0.02
highcut	E_{cut} [keV]	8.3 ± 0.2
	E_{fold} [keV]	20.4 ± 0.5
gaussian	EW_{Fe} [eV]	30 ± 12
	σ_{Fe} [keV]	$0.20^{p}_{-0.09}$
constant	$\text{const}_{\text{FPMB}}$	0.994 ± 0.004
	$\text{Flux}_{3-79 \text{ keV}}^b$ [$10^{-11} \text{ erg s}^{-1} \text{ cm}^{-2}$]	49.3 ± 0.3
	$\chi^2/\text{d.o.f.}$	418.1/351

Notes. The uncertainties are given at the 68.3% (1σ) confidence level and were obtained using the `error` command in `XSPEC` with $\Delta\chi^2 = 1$ for one parameter of interest. ^(b) Bolometric (unabsorbed) flux in the 3–79 keV range. ^(p) The symbol p denotes that the parameter hits its upper boundary.

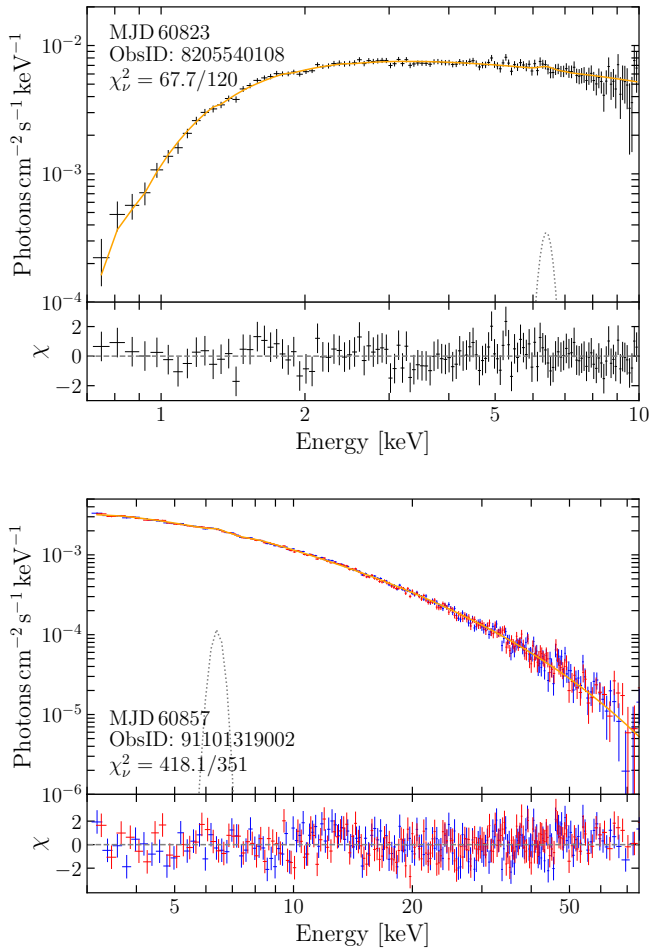


Fig. 4. Spectral composition of a representative phase-averaged NICER spectrum and the NuSTAR spectrum. *Upper panel:* The NICER data are fitted with the model $\text{TBabs} \times (\text{cutoffpl} + \text{gaussian})$. The solid orange line represents the best-fitting model, while the dotted grey line indicates the Gaussian component at 6.4 keV. *Lower panel:* The NuSTAR data are fitted with the model $\text{TBabs} \times (\text{powerlaw} \times \text{highcut} + \text{gaussian})$. The blue and red crosses denote FPMA and FPMB data, respectively. The solid orange line represents the best-fitting model, and the dotted grey line indicates the Gaussian component at 6.4 keV.

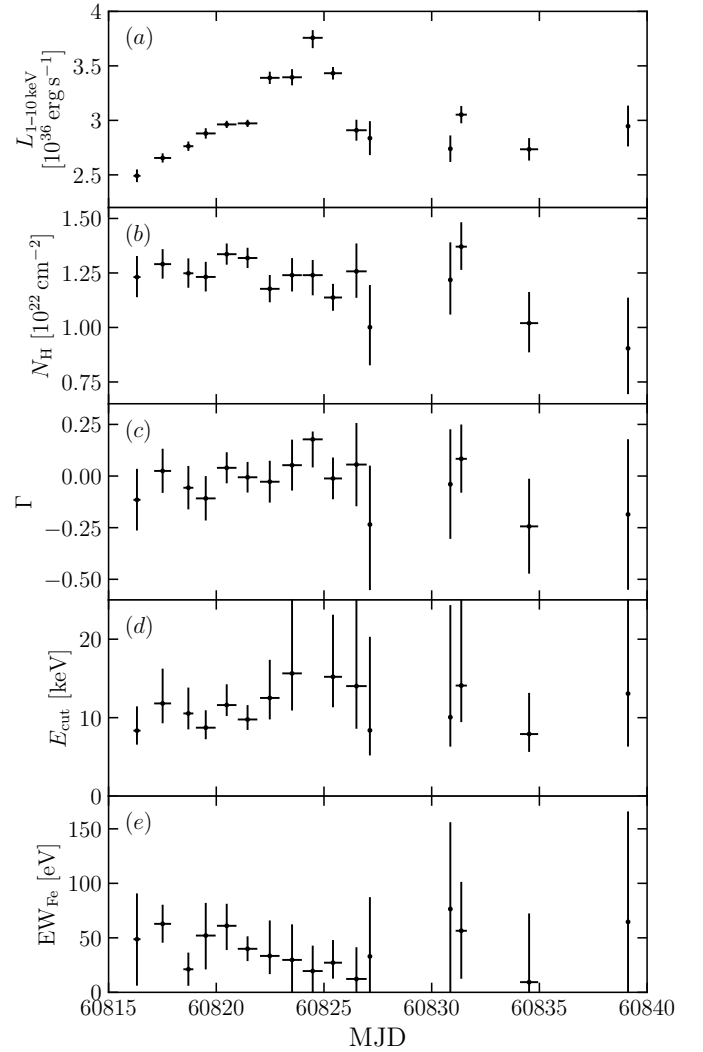


Fig. 5. Evolution of the key parameters of 2S 1417–624 obtained from NICER phase-averaged spectral analysis as a function of time. The panels present, from (a) to (e): the 1–10 keV luminosity assuming a distance of 7.4 kpc; the equivalent hydrogen column density N_{H} of the interstellar medium; the photon index Γ and cut-off energy E_{cut} of the continuum; and the equivalent width of the iron $\text{K}\alpha$ line at 6.4 keV.

3.2.2. Phase-resolved spectral analysis

To investigate spectral variability as a function of rotational phase, we performed phase-resolved spectroscopy of the NICER

and NuSTAR data. This method enables the examination of changes in the continuum shape and line features across the pulse profile, offering insights into the geometry and emission mechanisms of the system. The pulse phase was computed using the ephemerides listed in Table 2 according to

$$\phi = \frac{1}{P}(t - t_0) - \frac{1}{2} \frac{\dot{P}}{P^2}(t - t_0)^2, \quad (1)$$

where P is the pulse period, \dot{P} its time derivative at the reference epoch t_0 , with t_0 also defining the zero phase. The data were divided into ten equally spaced phase bins, with source spectra and background spectra extracted using the corresponding GTIs. Each spectrum was fitted with the same model used in the phase-averaged analysis to trace the evolution of the emission components over the pulsation cycle.

In Fig. 6, we show the key parameters of the phase-resolved spectra along with their averaged values in each phase bin, in order to examine their modulation with pulse phase. With the exception of the equivalent hydrogen column density, the spectral parameters generally exhibit no significant phase-dependent variations.

For the NuSTAR observation, the 32.5 ks exposure provides sufficient statistics to carry out phase-resolved spectral analysis over a broad energy range, with the results shown in Fig. 7. The spectral parameters of the different components exhibit clear variations with pulse phase.

We note that the pulse-phase variations are partly driven by degeneracies among parameters such as N_H , Γ , and E_{cut} . In this context, N_H mainly acts to adjust the slope of the low-energy continuum rather than to represent genuine interstellar absorption, particularly in the NuSTAR observation. In most cases, the iron line appears weak, and its strength is poorly constrained.

3.3. Polarimetric analysis

The exploratory polarimetric analysis of 2S 1417–624 was carried out in *XSPEC*, fully accounting for both energy dispersion and the source’s spectral shape. Stokes I , Q , and U spectra were first extracted from the two available DUs, following the methods in Sect. 2.2. All six spectra were then fitted simultaneously with *XSPEC*.

The source continuum is well described by an absorbed cut-off power-law. Given IXPE’s soft X-ray sensitivity, we adopted a simple phenomenological model:

`constant × TBabs × powerlaw × polconst`,

where `constant` accounts for cross-calibration between the two DUs, with the DU1 factor fixed at unity. The `polconst` component is used to model polarization, assuming an energy-independent PD and PA. This setup was applied to both phase-averaged and phase-resolved analyses.

Finally, the model-independent `pcube` method was employed as a reference to the *XSPEC* results, since the two approaches are expected to produce consistent outcomes. We calculated the normalized Stokes parameters $q = Q/I$ and $u = U/I$, the PD as $\text{PD} = \sqrt{q^2 + u^2}$, and the PA as $\text{PA} = \frac{1}{2} \arctan(u/q)$, measured counterclockwise from north to east on the sky (Kislat et al. 2015).

3.3.1. Phase-averaged polarimetric analysis

A phase-averaged analysis of the IXPE observation over the full 2–8 keV band was conducted, with the results presented in Table 4. The polarization degree was measured to be $3.3 \pm 1.7\%$,

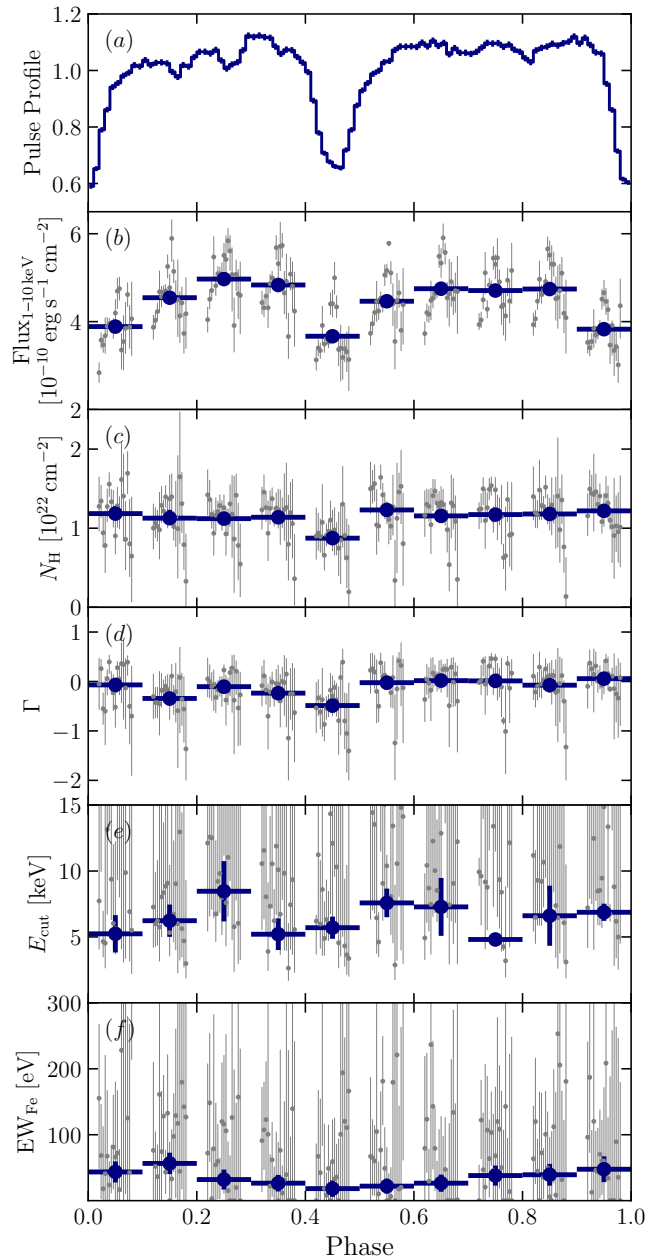


Fig. 6. Phase-dependent parameters of 2S 1417–624 obtained from NICER phase-resolved spectral analysis. The panels show, from (a) to (f): the normalized pulse profile measured by NICER; the unabsorbed flux in 1–10 keV; the equivalent hydrogen column density N_H of the interstellar medium; the photon index Γ and the cut-off energy E_{cut} of the continuum; and the equivalent width of the iron $K\alpha$ line at 6.4 keV. Grey dots indicate measurements from the phase-resolved spectral analysis of individual observations (slightly offset for clarity), while navy dots represent the average parameter values in each phase bin.

with a corresponding polarization angle of $18^\circ \pm 15^\circ$. Assuming a source distance of $d \approx 7.4$ kpc (Bailer-Jones et al. 2021), the luminosity of 2S 1417–624 at the end of the outburst is estimated at $L \approx 6.1 \times 10^{35} \text{ erg s}^{-1}$ in the 2–8 keV band.

We then investigated the energy dependence of the polarization properties of 2S 1417–624 by conducting an energy-resolved polarimetric analysis. The data were divided into five energy intervals: 2–3, 3–4, 4–5, 5–6, and 6–8 keV. Fitting was performed in *XSPEC*, using all bins within the 2–8 keV range for the Stokes I spectra, while for the Stokes Q and U spectra, bins

Table 4. Best-fit spectral parameters obtained from the phase-averaged spectro-polarimetric analysis of the IXPE data using `xsPEC`.

Component	Parameter	Value
TBabs	N_{H} [10^{22} cm^{-2}]	$3.38^{+0.17}_{-0.16}$
powerlaw	Γ	0.86 ± 0.04
polconst	PD [%]	3.3 ± 1.7
	PA [deg]	18 ± 15
constant	const _{DU3}	1.012 ± 0.008
	Flux _{2–8 keV} ^a [$10^{-11} \text{ erg s}^{-1} \text{ cm}^{-2}$]	7.93 ± 0.07
	$\chi^2/\text{d.o.f.}$	734.6/795

Notes. The uncertainties are given at the 68.3% (1σ) confidence level and were obtained using the `error` command in `xsPEC` with $\Delta\chi^2 = 1$ for one parameter of interest. ^(a) Observed (absorbed) flux in the 2–8 keV range.

Table 5. Polarimetric parameters in different energy bins for the IXPE observations with `xsPEC` method and `pcube` method.

Energy [keV]	PD _{xsPEC} [%]	PA _{xsPEC} [deg]	PD _{pcube} [%]	PA _{pcube} [deg]
2–3	4.3 ± 3.5	1 ± 27	$3.2^{+3.5}_{-3.2}$	9 ± 31
3–4	$1.5^{+3.0}_{-1.5}$	73^{\dagger}	$2.2^{+2.9}_{-2.2}$	64 ± 38
4–5	$2.6^{+3.7}_{-2.6}$	29^{\dagger}	$2.3^{+3.5}_{-2.3}$	22 ± 44
5–6	13.9 ± 4.7	21 ± 10	13.6 ± 4.5	20 ± 9
6–8	$5.2^{+5.4}_{-5.2}$	-9^{\dagger}	7.0 ± 5.8	-7 ± 24
2–8	3.3 ± 1.7	18 ± 15	4.4 ± 2.3	12 ± 15

Notes. The uncertainties computed using the `error` command are given at the 68.3% (1σ) confidence level ($\Delta\chi^2 = 1$ for one parameter of interest). ^(†) The PA cannot be confined within the 1σ confidence level; therefore, we present the most probable value instead.

outside the respective energy range of interest were excluded. The results are presented in Table 5. For comparison, we also applied the model-independent `pcube` algorithm, with the corresponding results listed in Table 5 as well, showing broadly consistent outcomes.

Except for the 5–6 keV interval, most energy bins exhibit no significant polarization. The reduced PD in the phase-averaged data can be partially attributed to the phase dependence of the PA. Nevertheless, the relatively high polarization observed in the 5–6 keV band is noteworthy, particularly since no additional spectral component is detected within this energy range.

3.3.2. Phase-resolved polarimetric analysis

Investigating the phase-dependent properties of pulsars is essential, as their geometry evolves with rotation. Using the ephemerides listed in Table 2, the phase of each photon event is calculated by Eq. 1. The photons were divided into six phase bins, arranged such that each main peak was represented by three bins containing comparable photon counts. For each phase bin, Stokes I , Q , and U spectra were generated following the procedure described in Sect. 2.2.

We first applied the `xsPEC` method to each phase bin, restricting the analysis to the 2–8 keV energy range. The results for the combined data set are summarized in Table 6 and illustrated in Fig. 8. Polarization is detected at a significance level exceeding 1σ in only half of the phase bins; however, the variation in PA between the last two bins indicates that the modulation of PA with pulse phase remains discernible despite the incomplete phase coverage.

The `pcube` algorithm was then applied to the phase-resolved data, with the results presented in the last two columns of Table 6. In general, the PD values derived from `pcube` are higher than those obtained with `xsPEC`, whereas the PAs from both approaches are typically consistent when the corresponding PD measurements are significant.

4. Discussion

4.1. The rotating vector model and the geometry of the pulsar

In Sect. 3.3.2, we showed that the PA varies with phase, at least in the last two phase bins. Although the constraints in the remaining bins are weak, we aim to explore whether some geometrical parameters can still be derived under the RVM (Radhakrishnan & Cooke 1969; Meszaros et al. 1988; Poutanen 2020), which has been successfully applied to several XRPCs observed by IXPE (see e.g., Doroshenko et al. 2022; Tsygankov et al. 2022; Mush-tukov et al. 2023; Marshall et al. 2022; Tsygankov et al. 2023; Malacaria et al. 2023; Doroshenko et al. 2023; Suleimanov et al. 2023; Heyl et al. 2024; Zhao et al. 2024; Forsblom et al. 2024, 2025; Loktev et al. 2025). In brief, when the emission is dominated by ordinary-mode (O-mode) photons, the RVM predicts that the PA follows Eq. (30) from Poutanen (2020):

$$\tan(\text{PA} - \chi_p) = \frac{-\sin \theta \sin(\phi - \phi_0)}{\sin i_p \cos \theta - \cos i_p \sin \theta \cos(\phi - \phi_0)}, \quad (2)$$

where χ_p is the position angle of the pulsar angular momentum measured from north to east, i_p is the inclination of the NS angular momentum to the line of sight, θ is the angle between the spin axis and the magnetic dipole, and ϕ_0 indicates the phase when the northern magnetic pole passes in front of the observer.

If the observed radiation is dominated by the extraordinary mode (X-mode), the position angle of the pulsar’s angular momentum is given by $\chi_p \pm 90^\circ$. In the non-relativistic case, the PA is independent of the polarization degree of the radiation emerging from the neutron star surface.

The distribution of PA deviates from a normal distribution, particularly when the PD is low. Therefore, we adopted the probability density function of the PA, ψ , as derived by Naghizadeh-Khouei & Clarke (1993):

$$G(\psi) = \frac{1}{\sqrt{\pi}} \left\{ \frac{1}{\sqrt{\pi}} + \eta e^{\eta^2} [1 + \text{erf}(\eta)] \right\} e^{-p_0^2/2}, \quad (3)$$

where $p_0 = \text{PD}/\text{PD}_{\text{err}}$ is the measured PD in units of its error, $\eta = p_0 \cos[2(\psi - \psi_0)] / \sqrt{2}$, and ψ_0 is the expectation value of PA. Here, erf denotes the error function.

Table 6. Spectro-polarimetric measurement for different pulse-phase bins of 2S 1417–624 from the IXPE observation, derived using *xspect* and *pcube*.

Phase	N_{H} [10^{22} cm^{-2}]	Γ	PD _{xspect} [%]	PA _{xspect} [deg]	$\chi^2/\text{d.o.f.}$	PD _{pcube} [%]	PA _{pcube} [deg]
0.00–0.15	$2.84^{+0.45}_{-0.44}$	0.75 ± 0.10	$2.7^{+4.6}_{-2.7}$	-28^\dagger	485.9/480	7.0 ± 6.3	10 ± 26
0.15–0.30	$3.21^{+0.43}_{-0.42}$	$0.75^{+0.10}_{-0.09}$	7.5 ± 4.2	8 ± 17	459.2/516	7.7 ± 5.8	-15 ± 28
0.30–0.45	3.44 ± 0.44	$0.73^{+0.10}_{-0.09}$	$2.2^{+4.2}_{-2.2}$	90^\dagger	494.6/519	6.8 ± 5.7	69 ± 24
0.45–0.62	$3.46^{+0.40}_{-0.39}$	0.95 ± 0.09	3.9 ± 3.9	-78^\dagger	520.4/525	6.3 ± 5.3	-59 ± 24
0.62–0.80	$3.04^{+0.39}_{-0.38}$	0.79 ± 0.09	11.2 ± 3.8	-3 ± 10	509.7/537	15.8 ± 5.3	-4 ± 10
0.80–1.00	$3.63^{+0.38}_{-0.37}$	$0.99^{+0.09}_{-0.08}$	11.2 ± 3.8	45 ± 10	495.2/543	12.3 ± 5.2	41 ± 12

Notes. The uncertainties in the spectro-polarimetric parameters, computed using the `error` command in *xspect*, are provided at the 68.3% (1σ) confidence level ($\Delta\chi^2 = 1$ for one parameter of interest). The right two columns give PD and PA estimated with the *pcube* algorithm and the uncertainties given at the 1σ confidence level. ^(†) The PA cannot be confined within the 1σ confidence level; therefore, we presented the most probable value instead.

Table 7. Best-fit RVM parameters for 2S 1417–624, derived from PAs measured with IXPE using the *xspect* and *pcube* methods. The fourth column also lists the parameters derived with the unbinned photon-by-photon method.

Parameter	<i>xspect</i>	<i>pcube</i>	unbinned method
χ_p [deg]	-54^{+46}_{-42}	-57^{+54}_{-38}	-88^{+51}_{-32}
θ [deg]	68^{+15}_{-27}	64^{+17}_{-27}	60^{+19}_{-25}
i_p [deg]	22^{+26}_{-16}	34^{+36}_{-26}	21^{+22}_{-14}
$\phi_0/2\pi$	$0.08^{+0.16}_{-0.21}$	$0.09^{+0.18}_{-0.16}$	$-0.05^{+0.16}_{-0.10}$

The best-fit RVM parameters are obtained by maximizing the likelihood function $\log L = \sum \log G(\psi)$. To explore the parameter space, we employ the Markov Chain Monte Carlo (MCMC) ensemble sampler implemented in the *UltraNest* package (Buchner 2021) to compute the posterior distributions of the four free RVM parameters. The resulting best-fit values from PAs derived by both the *xspect* and *pcube* methods are summarized in Table 7. We show the corresponding covariance plots using the *xspect* method in Fig. 9 and the best-fit RVM curve to the measured PAs in Fig. 8. The parameter distributions obtained from the two methods are broadly consistent.

We also applied the unbinned photon-by-photon method to fit the RVM (González-Caniulef et al. 2023), assuming a variable PA across the pulse phase but a constant PD. The results are shown in the last column of Table 7 and Fig. 10. They are consistent, within uncertainties, with those obtained from the binned PA fitting using the *xspect* and *pcube* methods. We note, however, that the instrument’s effective area is not accounted for in this approach. Since the IXPE effective area peaks at ~ 2 keV, most of the detected photons are concentrated in this energy range, which may introduce a bias in the fit.

Although subject to considerable uncertainties, the RVM fit suggests that 2S 1417–624 possesses a large magnetic obliquity, compatible with a quasi-orthogonal geometry, though smaller obliquities cannot be entirely ruled out. The ϕ_0 angle, which denotes the phase at which the northern magnetic pole comes closest to the observer, is well constrained to be near phase zero, coinciding with the main dip in the pulse profile. Such a geometry approaches that of an orthogonal rotator, an extreme case of pulsar configuration that gives rise to the most pronounced emission and polarization signatures, and is therefore of fundamental importance for probing the magnetic field structure, radiation mechanisms, and geometrical evolution of neutron stars.

4.2. A more detailed polarimetric investigation in the 5–6 keV band

As shown in Sect. 3.3.1, the 5–6 keV band exhibits notably stronger polarization than the other energy bands. This could be due either to photons in this band generally having a much higher PD while remaining consistent with the PA modulation observed in other energy bands, or to the PA in the 5–6 keV band exhibiting weaker modulation across the pulse phase, thereby indicating an energy dependence of the PA. However, in our case, the insufficient photon counts within the IXPE observation do not support a full phase–energy–resolved polarimetric analysis. Instead, we can only investigate the behavior of the 5–6 keV band by comparing it directly with the photons in the other bands combined. Specifically, we use the *xspect* method to compute PAs and PDs in different phase bins within the 5–6 keV band and in the energy range excluding 5–6 keV, and the results are shown in Fig. 11. We find that the phase-resolved PDs in the 5–6 keV band are generally higher than those in the energy range excluding 5–6 keV, particularly in the phase bins 0.15–0.30 and 0.80–1.00. Moreover, in most phase bins, the PAs derived for the two energy bands are consistent within their uncertainties. The only notable exception is the 0.45–0.62 phase bin, where the PA differs by approximately 60° .

At present, there is no theoretical model that can account for such an abrupt PA swing between two energy bands whose photon energies lie well below the cyclotron energy. A comparable phenomenon has been reported in 4U 1907+09 (Zhou et al. 2025), where a PA swing of approximately 90° was marginally detected between two adjacent energy bands within a single phase bin. It is worth noting that both cases were observed under photon-starved conditions, where the limited photon statistics reduce the robustness of the measurements. Future observations with significantly improved photon statistics and broader energy coverage will be crucial for confirming these features and for providing the empirical basis needed to develop a physical explanation.

4.3. Possible scenario for the 2025 outburst of 2S 1417–624

The observed flux from NuSTAR is $\sim 4.93 \times 10^{-10} \text{ erg s}^{-1} \text{ cm}^{-2}$ (in the 3–79 keV band), which corresponds to a luminosity of $3.2 \times 10^{36} \text{ erg s}^{-1}$, assuming a source distance of 7.4 kpc (Bailer-Jones et al. 2021). Liu et al. (2024) reported a possible cyclotron line at 100 keV in this source, implying a magnetic field strength of $\sim 9 \times 10^{12} \text{ G}$. Given that accreting pulsars can op-

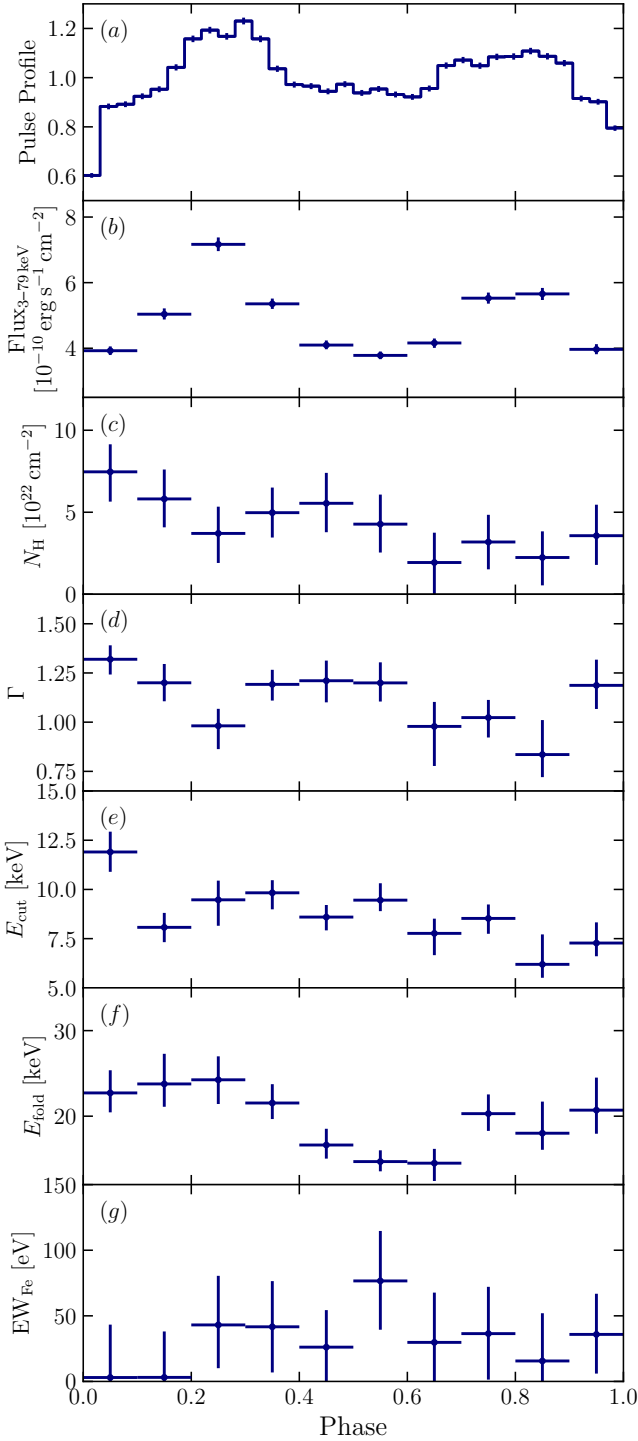


Fig. 7. Phase-dependent parameters of 2S 1417–624 obtained from NuSTAR phase-resolved spectral analysis using the model $\text{TBabs} \times (\text{powerlaw} \times \text{highcut} + \text{gaussian})$. The panels show, from (a) to (g): the normalized pulse profile measured in 3–79 keV with NuSTAR; the unabsorbed flux in 3–79 keV; the equivalent hydrogen column density N_{H} of the interstellar medium; the photon index Γ ; the cut-off energy E_{cut} , and the folding energy E_{fold} of the continuum; and the equivalent width of the iron $\text{K}\alpha$ line at 6.4 keV.

erate in different radiative regimes depending on their luminosity, the critical luminosities of this source are estimated to be $\sim 1.55 \times 10^{37} \text{ erg s}^{-1}$ and $\sim 5 \times 10^{37} \text{ erg s}^{-1}$, as determined using the approaches of Becker et al. (2012) and Mushtukov et al. (2015), respectively. Since the NuSTAR observation oc-

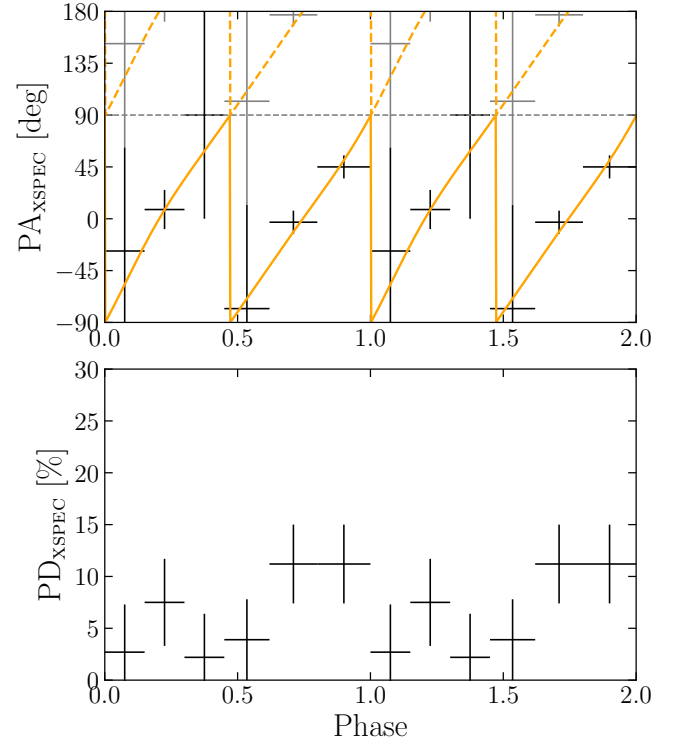


Fig. 8. Pulse-phase dependence of PA and PD in the 2–8 keV band derived using the *xspec* method. For PAs that cannot be constrained at the 1σ confidence level, the uncertainty is set to 90° . Some PAs are shown twice with an added offset of 180° to illustrate phase continuity. The orange solid curve denotes the best-fit RVM to the original PA measurements.

curred at the end of the outburst, the corresponding MAXI count rate was $\sim 0.025 \text{ cts/s}$, whereas the outburst peak reached a MAXI count rate of $\sim 0.1 \text{ cts/s}$, four times higher than during the NuSTAR observation. Therefore, the peak luminosity of the 2025 outburst can be roughly estimated as four times the NuSTAR luminosity: $L_{\text{peak}} \approx 4 \times L_{\text{NuSTAR}} = 1.3 \times 10^{37} \text{ erg s}^{-1}$. It is shown that even the peak luminosity did not exceed the critical luminosity; therefore, the radiation regime remained in the pencil-beam pattern throughout the entire outburst. The absence of significant luminosity-dependent changes in the pulse profile (as observed with NICER, IXPE, and NuSTAR) further supports this conclusion. We also note that the distance to this source may carry some uncertainty, which in turn affects the luminosity estimate. Liu et al. (2025) reported two characteristic flux levels associated with changes in the pulse profile, at $\sim 4.1 \times 10^{-9}$ and $6.4 \times 10^{-9} \text{ erg cm}^{-2} \text{ s}^{-1}$ (2–140 keV). Below $4.1 \times 10^{-9} \text{ erg cm}^{-2} \text{ s}^{-1}$, the emission is thought to be dominated by a pencil-beam pattern. Therefore, even though the peak flux of the 2025 outburst is about $F_{\text{peak}} \approx 2.0 \times 10^{-9} \text{ erg cm}^{-2} \text{ s}^{-1}$ (3–79 keV, equivalent to $4 \times F_{\text{NuSTAR}}$), it still lies below the threshold at which a transition in the radiation pattern is expected. (The difference in flux integration energy bands does not significantly affect this conclusion, as the broader energy band is not expected to further increase the measured flux substantially). Polarization measurements, which constrain the geometry of accreting pulsars, greatly enhance our understanding of the pulse profile. With $\theta \approx 64^\circ$, as determined by fitting PAs obtained by *xspec* and *pcube*, and also the unbinned method, the source is probably close to an orthogonal rotator configuration. Considering $i_p \approx 24^\circ$ from the same methods, and the relatively wide beam

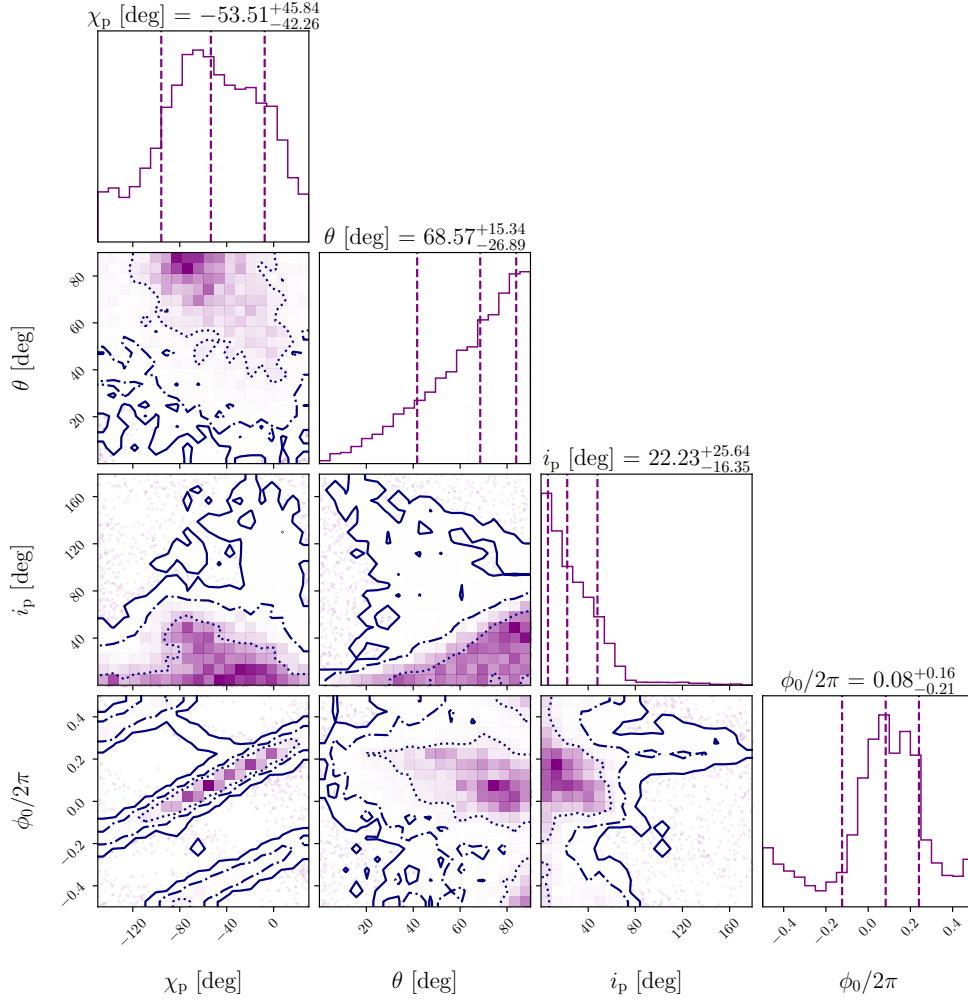


Fig. 9. Corner plot showing the posterior distributions of the RVM parameters describing the pulsar geometry, obtained from the PA values in the phase-resolved spectro-polarimetric analysis of the IXPE observation. The two-dimensional contours represent the 68.27%, 95.45%, and 99.73% confidence levels, while the histograms display the normalized one-dimensional distributions for each parameter derived from the posterior samples. The mean values and corresponding 1σ confidence intervals are indicated above each histogram, with the dashed lines marking these intervals.

angle of a pencil-beam emission pattern (Hu et al. 2023), it is plausible to observe two flux maxima within a single rotational cycle, consistent with the observed pulse profile.

5. Conclusions

The multi-mission campaign on 2S 1417–624 during its weak type-II outburst in 2025 has provided new insights into the source’s spectral and polarimetric properties. Phase-averaged and phase-resolved spectroscopy with NICER and NuSTAR shows that the spectra are well described by a power-law with a high-energy cut-off, with several parameters exhibiting systematic pulse-phase modulations indicative of changes in emission geometry. With IXPE, we obtained the first polarimetric measurements of this source, yielding a phase-averaged polarization degree of $3.3 \pm 1.7\%$ and a polarization angle of $18^\circ \pm 15^\circ$. Complementary phase-resolved polarimetric analysis suggests that 2S 1417–624 possesses a magnetic obliquity of $\theta = 64^{+17}_{-26}$ deg, indicating that the geometry is compatible with a quasi-orthogonal rotator within uncertainties, although lower obliquities cannot be excluded. Together, these results establish a consistent picture in which both the spectral and polarization properties vary significantly over the pulse cycle, offering im-

portant constraints on the geometry and emission processes in the accretion region of this transient XRP.

Acknowledgements. The Imaging X-ray Polarimetry Explorer (IXPE) is a joint US and Italian mission. The US contribution is supported by the National Aeronautics and Space Administration (NASA) and led and managed by its Marshall Space Flight Center (MSFC), with industry partner Ball Aerospace (contract NNM15AA18C). The Italian contribution is supported by the Italian Space Agency (Agenzia Spaziale Italiana, ASI) through contract ASI-OHBI-2022-13-I.0, agreements ASI-INAF-2022-19-HH.0 and ASI-INFN-2017.13-H0, and its Space Science Data Center (SSDC) with agreements ASI-INAF-2022-14-HH.0 and ASI-INFN 2021-43-HH.0, and by the Istituto Nazionale di Astrofisica (INAF) and the Istituto Nazionale di Fisica Nucleare (INFN) in Italy. This research used data products provided by the IXPE Team (MSFC, SSDC, INAF, and INFN) and distributed with additional software tools by the High-Energy Astrophysics Science Archive Research Center (HEASARC) at NASA Goddard Space Flight Center (GSFC). This research has been supported by the Deutsche Forschungsgemeinschaft (DFG) grants 549824807 (LD) and WE 1312/59-1 (VFS), and the UKRI Stephen Hawking fellowship (AAM). Pengju Wang is grateful for the financial support provided by the Sino-German (CSC-DAAD) Postdoc Scholarship Program (57678375).

References

Apparao, K. M. V., Naranan, S., Kelley, R. L., & Bradt, H. V. 1980, A&A, 89, 249

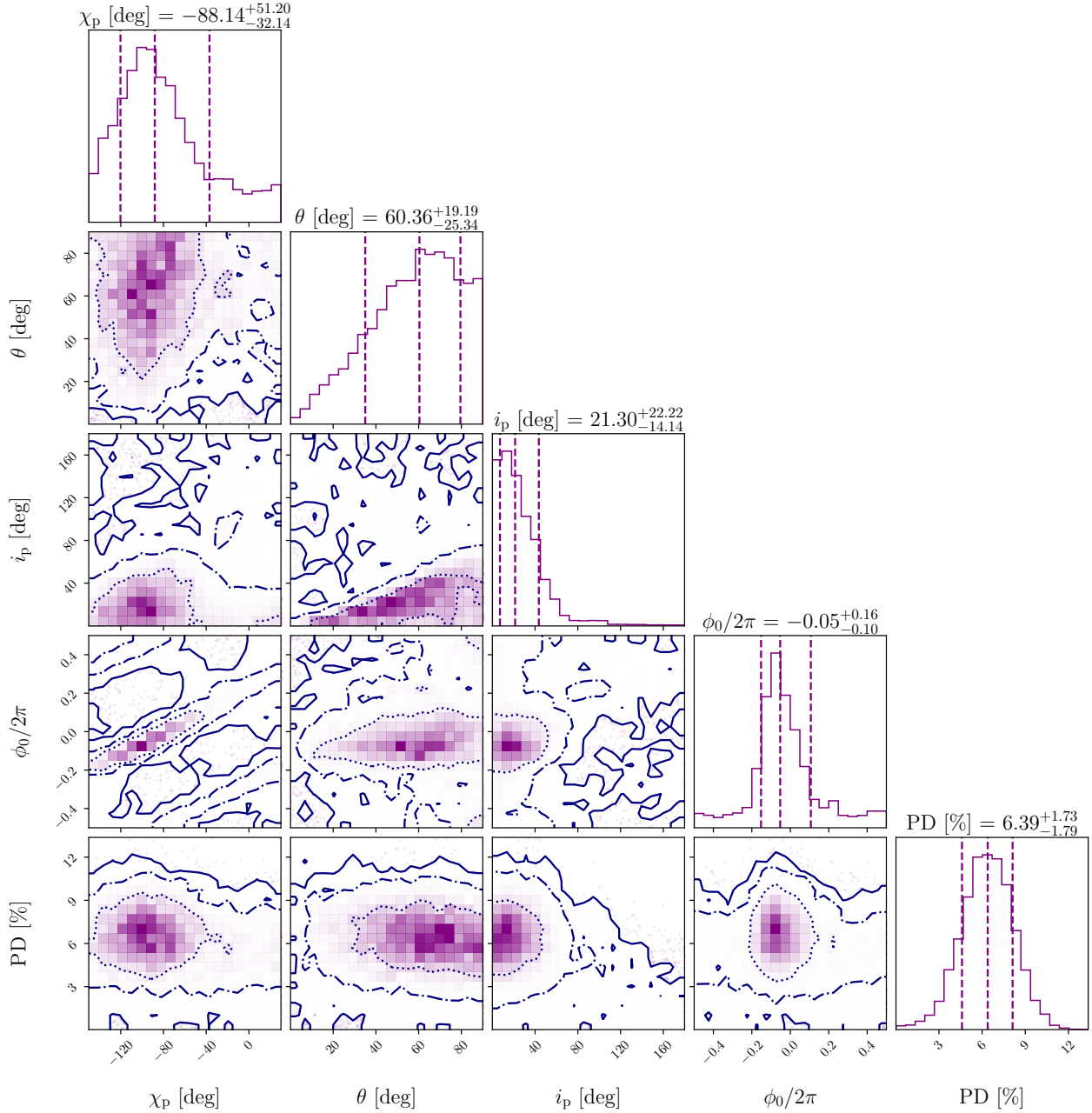


Fig. 10. Similar to Fig. 9, but showing the values derived from the unbinned photon-by-photon method.

Arnaud, K. A. 1996, in ASP Conf. Ser., Vol. 101, *Astronomical Data Analysis Software and Systems V*, ed. G. H. Jacoby & J. Barnes (San Francisco: Astron. Soc. Pac.), 17

Bailer-Jones, C. A. L., Rybizki, J., Fouesneau, M., Demleitner, M., & Andrae, R. 2021, *AJ*, **161**, 147

Bailer-Jones, C. A. L., Rybizki, J., Fouesneau, M., Mantelet, G., & Andrae, R. 2018, *AJ*, **156**, 58

Baldini, L., Barbanera, M., Bellazzini, R., et al. 2021, *Astroparticle Physics*, **133**, 102628

Baldini, L., Bucciantini, N., Lalla, N. D., et al. 2022, *SoftwareX*, **19**, 101194

Barthelmy, S. D., Barbier, L. M., Cummings, J. R., et al. 2005, *Space Sci. Rev.*, **120**, 143

Basko, M. M., & Sunyaev, R. A. 1975, *A&A*, **42**, 311

Becker, P. A., Klockhov, D., Schönherr, G., et al. 2012, *A&A*, **544**, A123

Buchner, R., Bennett, K., Bignami, G. F., et al. 1983, *A&A*, **128**, 245

Buchner, J. 2021, *The Journal of Open Source Software*, **6**, 3001

Di Marco, A., Costa, E., Muleri, F., et al. 2022, *AJ*, **163**, 170

Di Marco, A., Soffitta, P., Costa, E., et al. 2023, *AJ*, **165**, 143

Doroshenko, V., Poutanen, J., Tsygankov, S. S., et al. 2022, *Nature Astronomy*, **6**, 1433

Doroshenko, V., Poutanen, J., Heyl, J., et al. 2023, *A&A*, **677**, A57

Finger, M. H., Wilson, R. B., & Chakrabarty, D. 1996, *A&AS*, **120**, 209

Forsblom, S. V., Tsygankov, S. S., Suleimanov, V. F., Mushtukov, A. A., & Poutanen, J. 2025, *A&A*, **696**, A224

Forsblom, S. V., Tsygankov, S. S., Poutanen, J., et al. 2024, *A&A*, **691**, A216

Gendreau, K. C., Arzoumanian, Z., Adkins, P. W., et al. 2016, in *Proc. SPIE, Vol. 9905, Space Telescopes and Instrumentation 2016: Ultraviolet to Gamma Ray*, ed. J.-W. A. den Herder, T. Takahashi, & M. Bautz, 99051H

González-Caniulef, D., Caiazzo, I., & Heyl, J. 2023, *MNRAS*, **519**, 5902

Grindlay, J. E., Petro, L. D., & McClintock, J. E. 1984, *ApJ*, **276**, 621

Gupta, S., Naik, S., & Jaisawal, G. K. 2019, *MNRAS*, **490**, 2458

Gupta, S., Naik, S., Jaisawal, G. K., & Epili, P. R. 2018, *MNRAS*, **479**, 5612

Harrison, F. A., Craig, W. W., Christensen, F. E., et al. 2013, *ApJ*, **770**, 103

Hemphill, P. B., Rothschild, R. E., Cheatham, D. M., et al. 2019, *ApJ*, **873**, 62

Heyl, J., Doroshenko, V., González-Caniulef, D., et al. 2024, *Nature Astronomy*, **8**, 1047

Hu, Y. F., Ji, L., Yu, C., et al. 2023, *ApJ*, **945**, 138

Inam, S. Ç., Baykal, A., Matthew Scott, D., Finger, M., & Swank, J. 2004, *MNRAS*, **349**, 173

Ji, L., Doroshenko, V., Santangelo, A., et al. 2020, *MNRAS*, **491**, 1851

Kaastra, J. S., & Bleeker, J. A. M. 2016, *A&A*, **587**, A151

Kelley, R. L., Apparao, K. M. V., Doxsey, R. E., et al. 1981, *ApJ*, **243**, 251

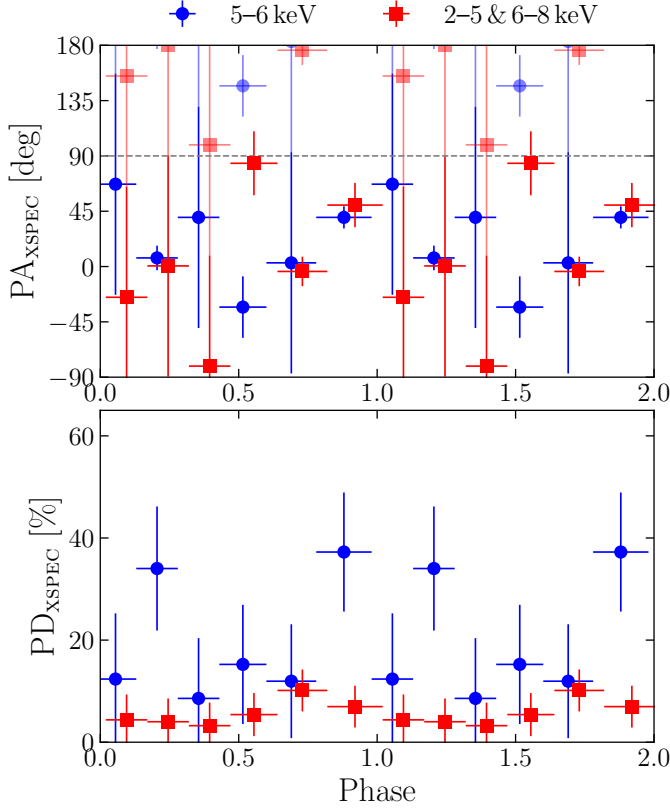


Fig. 11. Pulse-phase-resolved PAs and PDs in different energy bands obtained using the *xspec* method. Blue circles and red squares represent the measurements in the 5–6 keV band and in the energy range excluding 5–6 keV, respectively. For PAs that cannot be constrained at the 1σ confidence level, the uncertainty is set to 90° . For clarity, data points within the same phase bin are slightly offset, and some PAs are plotted with an added constant of 180° to illustrate their continuity with phase.

Kislat, F., Clark, B., Beilicke, M., & Krawczynski, H. 2015, *Astroparticle Physics*, **68**, 45
Kong, L. D., Zhang, S., Ji, L., et al. 2021, *ApJ*, **917**, L38
Liu, Q., Kong, L., Güngör, C., et al. 2025, *A&A*, **699**, A58
Liu, Q., Santangelo, A., Kong, L. D., et al. 2024, *A&A*, **691**, A215
Loktev, V., Forsblom, S. V., Tsygankov, S. S., et al. 2025, *A&A*, **698**, A22
Malacaria, C., Heyl, J., Doroshenko, V., et al. 2023, *A&A*, **675**, A29
Mandal, M., & Pal, S. 2022, *Ap&SS*, **367**, 112
Marshall, H. L., Ng, M., Rogantini, D., et al. 2022, *ApJ*, **940**, 70
Matsuoka, M., Kawasaki, K., Ueno, S., et al. 2009, *PASJ*, **61**, 999
Meszaros, P., Novick, R., Szentgyorgyi, A., Chanan, G. A., & Weisskopf, M. C. 1988, *ApJ*, **324**, 1056
Mushtukov, A., & Tsygankov, S. 2024, in *Handbook of X-ray and Gamma-ray Astrophysics*, ed. C. Bambi & A. Santangelo (Singapore: Springer), 4105
Mushtukov, A. A., Suleimanov, V. F., Tsygankov, S. S., & Poutanen, J. 2015, *MNRAS*, **447**, 1847
Mushtukov, A. A., Tsygankov, S. S., Poutanen, J., et al. 2023, *MNRAS*, **524**, 2004
Naghizadeh-Khouei, J., & Clarke, D. 1993, *A&A*, **274**, 968
Poutanen, J. 2020, *A&A*, **641**, A166
Poutanen, J., Tsygankov, S. S., & Forsblom, S. V. 2024, *Galaxies*, **12**, 46
Radhakrishnan, V., & Cooke, D. J. 1969, *Astrophys. Lett.*, **3**, 225
Reig, P., & Nespoli, E. 2013, *A&A*, **551**, A1
Serim, M. M., Özüdoğru, Ö. C., Dönmez, Ç. K., et al. 2022, *MNRAS*, **510**, 1438
Soffitta, P., Baldini, L., Bellazzini, R., et al. 2021, *AJ*, **162**, 208
Suleimanov, V. F., Forsblom, S. V., Tsygankov, S. S., et al. 2023, *A&A*, **678**, A119
Tsygankov, S. S., Doroshenko, V., Poutanen, J., et al. 2022, *ApJ*, **941**, L14
Tsygankov, S. S., Doroshenko, V., Mushtukov, A. A., et al. 2023, *A&A*, **675**, A48
Verner, D. A., Ferland, G. J., Korista, K. T., & Yakovlev, D. G. 1996, *ApJ*, **465**, 487
Wang, P. J., Kong, L. D., Zhang, S., et al. 2022, *ApJ*, **935**, 125
Weisskopf, M. C., Soffitta, P., Baldini, L., et al. 2022, *JATIS*, **8**, 026002
Wilms, J., Allen, A., & McCray, R. 2000, *ApJ*, **542**, 914
Zhao, Q. C., Li, H. C., Tao, L., et al. 2024, *MNRAS*, **531**, 3935
Zhou, M., Ducci, L., Liu, H., et al. 2025, *arXiv e-prints*, arXiv:2507.17873